Tribology International 216 (2026) 111579

Contents lists available at ScienceDirect

Tribology International

journal homepage: www.elsevier.com/locate/triboint

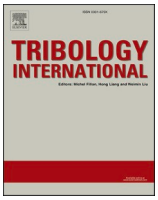

Skid resistance assessment of wet asphalt runways by coupling finite element simulation with real texture evolution data

Yunhong Yu [a], Houzhi Wang [a], You Wu [b], Haopeng Wang [c], Yixin Zhou [a], Jun Yang [a,*], Wei Huang [a]

[a] School of Transportation, Southeast University, Nanjing 211189, PR China
[b] Faculty of Civil Engineering and Geosciences, Delft University of Technology, the Netherlands
[c] Department of Civil and Environmental Engineering, University of Liverpool, Liverpool L69 3BX, UK

ARTICLE INFO

Keywords:
Finite element model
Hydroplaning
Real texture
Skid resistance
Runway

ABSTRACT

Adequate runway friction capacity during aircraft landing is crucial for flight safety. Accurately evaluating skid resistance under realistic service conditions remains a key challenge for maintaining flight safety. This study proposes a comprehensive skid resistance evaluation method that integrates laboratory testing with finite element simulation. A refined tire-pavement-fluid coupled model was developed, incorporating measured and series-generated worn texture data as key geometric boundary conditions in numerical analysis. The coupled effects of runway texture state, tire kinematics, and water film thickness on skid resistance were systematically investigated. Results suggest that runway macrotexture plays a vital role in maintaining skid resistance, with Stone Mastic Asphalt (SMA) mixtures providing superior skid resistance compared to Asphalt Concrete (AC) mixtures. As runway wear progresses, the combined influence of high speed and thick water films significantly increases the risk of hydroplaning and extends braking distance. This study highlights the significant effects of speed, water film thickness, and texture evolution on runway friction, offering theoretical guidance for material selection and safety evaluation of airport pavements.

1. Introduction

With the rapid growth of the air transportation industry, the frequency of aircraft takeoffs and landings has increased significantly, making landing safety a key focus in aviation safety research. Statistics show that runway excursions during landing account for a substantial proportion of aviation incidents. The International Civil Aviation Organization (ICAO) has classified such events as high-risk accident types [1].

Such high-risk incidents are closely related to pavement surface characteristics [2,3]. With increasing aircraft operations, runway surfaces are subjected to repeated shear forces from tires, leading to progressive texture degradation. This wear reduces the effective friction between the tire and runway, directly reducing skid resistance. Moreover, wet runway conditions severely compromise the effectiveness of aircraft braking. Research has shown that landing distances on wet runways are at least 1.4–2.1 times longer than on dry surfaces [4,5]. Therefore, precise evaluation of skid resistance becomes imperative for ensuring aircraft landing safety [6].

The complex interactions of water film depth, high-speed movement, and braking create analytical challenges for comprehensive theoretical modelling [7]. Additionally, due to the specific constraints of airport operations, field testing is both challenging and costly. Experimental equipment limitations constrain the precise measurement of dynamic tire-pavement contact and friction variations. Given these constraints, numerical simulation has become a practical approach to evaluate safety concerns related to aircraft landing [8–10]. Its primary advantage lies in the ability to precisely simulate the complex interactions among tire-pavement contact, tire-fluid interaction, and fluid-pavement interaction [11].

Fwa and Ong employed finite element (FE) software to simulate the interactions among smooth tires (i.e., slick tires without grooves), fluid, and pavement, analyzing the variation in tire footprint shape with speed [11,12]. Their work validated the National Aeronautics and Space Administration (NASA) hydroplaning equation and field-measured skid resistance data, demonstrating the feasibility of finite element modeling for predicting pavement friction. Tire design is one of the key factors influencing skid resistance. Zhu investigated a simplified patterned tire model to examine the effects of transverse groove parameters on friction

* Corresponding author.
E-mail address: yangjun@seu.edu.cn (J. Yang).

https://doi.org/10.1016/j.triboint.2025.111579
Received 12 August 2025; Received in revised form 12 December 2025; Accepted 13 December 2025
Available online 14 December 2025

Nomenclature

A_{ref}	reference wing area
a_b	braking acceleration
C_L	lift coefficients
C_D	drag coefficients
c_0	speed of sound in the fluid
F	total frictional force in the tire-runway contact area
F_z	vertical load
H	hurst exponent
M	aircraft mass
p	hydrodynamic pressure
R	effective rolling radius of the tire
$S(\omega)$	power spectral density
s	Hugoniot slope coefficient
T	braking duration
V_{land}	landing speed of the aircraft
v_{eq}	equivalent sliding velocity used in the theoretical formulation
v_s	sliding velocity
$v(t)$	instantaneous velocity during braking
$\langle z_p \rangle$	the mean deformation amplitude of the rubber contact surface
σ_0	average normal stress within the contact region
η	dynamic viscosity
ρ_0	the initial density of the water
ρ_a	air density
ω	angular frequency
ω_{min}	the minimum angular frequency
ω_{max}	the maximum angular frequency
ω_t	angular velocity of the tire
Γ_0	initial value of the material parameter
$\xi_{\parallel}$	horizontal correlation length
$\xi_{\perp}$	vertical correlation length

performance [13]. In addition, various geometric parameters-such as the depth and number of longitudinal grooves [14,15], groove shape [16], and groove width [17,18], have been shown to affect the contact pressure distribution between tire and pavement. Some studies also explored the influence of tire inflation pressure and axle load on the contact area [19,20]. Consider the braking system, some researchers introduced anti-lock braking systems (ABS) and slip ratio (SR) [21] to simulate dynamic skid resistance behavior under actual braking conditions. Key operational parameters such as vehicle speed and water film thickness have also been considered [22,23]. In terms of runway characteristics, factors such as pavement pressure distribution [24], hydrodynamic pressure, and water film distribution features [25] have been used to reveal how texture affects friction performance. Regarding pavement texture, the inherent complexity and randomness of surface morphology have led many researchers to simplify the pavement model in tire-pavement interaction analyses [26,27]. In some studies, the pavement was even idealized as a smooth surface without texture [28]. However, such simplifications cannot capture the stochastic nature and spatial variability of real pavement texture. To improve modeling accuracy, non-contact scanning technologies have been introduced to obtain three-dimensional texture profiles [29–31]. Some researchers employed CT scanning to reconstruct 3D pavement models for finite element analysis [32,33], but the limited resolution of CT often results in distortion of the reconstructed texture. By contrast, laser texture scanners, owing to their higher precision and measurement stability, have gradually become the preferred method for acquiring realistic 3D pavement textures [9,34]. Additionally, parametric algorithms have been proposed to simulate the wear and deterioration of runway textures during service, such as the texture evolution method developed by Zhu et al. [35].

However, the degradation process of real runway texture is far more complex than the wear patterns calculated by idealized algorithms. In-service texture evolution involves multiple interacting mechanisms, such as aggregate abrasion, material breakage, and morphological reconstruction [36,37]. The resulting degradation behavior differs substantially from the simplified wear patterns produced by algorithm-based simulations. As a consequence, existing numerical models generally lack texture-evolution inputs that can represent the actual deterioration occurring during runway service. This limited ability to characterize realistic texture evolution also highlights a deeper issue: experimental and numerical studies remain isolated from each other. Specifically, experimental tests can capture changes in texture morphology. However, they are often restricted to dry conditions and therefore cannot directly assess friction performance under wet surfaces.

Table 1
Geometric parameters of aircraft tire.

Diameter (mm)	Width (mm)	Groove depth (mm)	Groove width (mm)	Number of grooves
1220	420	9	10	4

Numerical simulations, although suitable for mechanistic and parametric analyses, rely on static textures or simplified surface models and thus fail to reflect the dynamic evolution of texture under repeated loading. Therefore, a systematic and integrated skid-resistance evaluation framework is needed-one that combines the strengths of both experiments and simulations and spans the entire service life of pavement.

Therefore, this study establishes a comprehensive skid resistance evaluation framework that covers the entire texture degradation process by integrating experimental data and numerical modeling. A high-resolution laser texture scanner was employed to systematically capture the true three-dimensional texture evolution of asphalt runway surfaces. The acquired experimental data was incorporated into a friction model, and imported directly into the finite element model as key geometric boundary conditions. By analyzing tire-runway contact interactions on progressively worn runway surfaces under wet conditions, the research systematically investigates the coupled effects of runway texture degradation, tire kinematics, and water film thickness on skid resistance performance. Furthermore, braking distances under different operating conditions were evaluated to provide quantitative references for runway safety during aircraft landing.

2. The tire-water-runway interaction model

2.1. Modeling of the tire

This study selected the commonly used aircraft tire type, 49 × 17, representative of those used on Boeing 747 and Airbus A320 aircraft. The primary geometric parameters of the tire are listed in Table 1. The two-dimensional cross-sectional view of the tire structure is shown in Fig. 1(a), which was constructed using the structural information reported in the literature [38]. The tire is primarily composed of rubber and cord materials. The rubber components include the apex rubber, sidewall rubber, carcass rubber, inner liner rubber, and tread. The main structural support is provided by the cord layers and the bead located at the edge of the sidewall. As illustrated in Fig. 1(b), the cross-section presents the internal structure and key components of the tire.

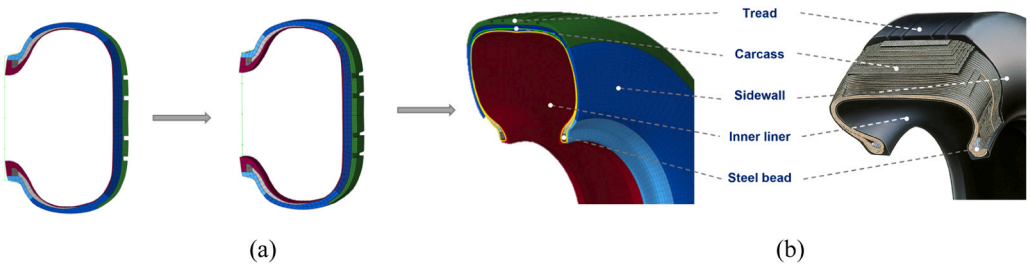

Fig. 1. Tire model (a) two-dimensional cross-section, (b) partial three-dimensional FE model.

Table 2
Yeoh model parameters for aircraft tire rubber.

	C_{10} (MPa)	C_{20} (MPa)	C_{30} (MPa)	Density(kg/m^3)
Tread	1.20	-0.78	0.094	1090
Sidewall	0.49	-0.40	0.083	1100
Carcass rubber	1.44	-0.25	0.016	1180
Apex rubber	1.62	-0.11	0.079	1260
Inner liner rubber	0.98	-0.13	0.028	1280

Rubber materials exhibit hyperelastic behavior characterized by strain energy potential functions. In this study, the Yeoh model was adopted to describe the deformation behavior of the rubber material [39]. The strain energy potential U is defined as follows [40]:

$$U = C_{10}(\bar{I}_1 - 3)^1 + C_{20}(\bar{I}_1 - 3)^2 + C_{30}(\bar{I}_1 - 3)^3 \quad (1)$$

Where U represents the strain energy density (MPa), $\bar{I}_1$ is the first deviatoric strain invariant (dimensionless). C_{10}, C_{20}, C_{30} denote temperature-sensitive coefficients, with the same units as U. The Yeoh model parameters for the aircraft tire rubber, obtained through uniaxial tensile testing, are listed in Table 2.

The cord-reinforced layers serve as the primary load-bearing components of the aircraft tire during operation. In this study, Rebar elements in ABAQUS were used to embed the cord structure within the rubber matrix, enabling the simulation of the interaction between the cords and the rubber material. For the tire modeling process, a two-dimensional axisymmetric cross-section was first constructed. This section was then meshed using Hypermesh (Fig. 1(a)). Finally, the two-dimensional model was imported into ABAQUS and revolved 360 ° to generate the full three-dimensional tire model (Fig. 1(b)).

2.2. Runway surface model

The asphalt mixtures used in this study were AC-16 and SMA-13, which are widely applied in airport pavements. Their gradation compositions are shown in Table 3. Considering the heavy load conditions of airport operations, epoxy-modified asphalt was selected, with an asphalt-aggregate ratio of 5.5 %. The epoxy system consisted of epoxy and curing agent in a 56:44 ratio, and the epoxy resin was blended with base asphalt at a 1:1 ratio.

A self-designed indoor accelerated wear device was used to apply loading to the asphalt mixtures [37,41]. The device consists of a rotating steel wheel, a servo-controlled loading system, and a temperature-controlled chamber. The wear stages were set to 0, 10,000, 20,000, 30,000, 40,000, and 50,000 wheel passes. The contact pressure of the wear testing device was set to 1.5 MPa to simulate aircraft loading conditions. The loading frequency is approximately 40 loading cycles

Table 3
Mass percentage (%) through each mesh (mm).

Sieve Size/mm	19	16	13.2	9.5	4.75	2.36	1.18	0.6	0.3	0.15	0.075
SMA-13		100	94.63	64.10	28.41	20.50	17.45	15.98	13.66	11.77	10.15
AC-16	100.0	99.9	90.9	67.6	46.9	35.6	25.2	19.0	12.1	9.9	6.1

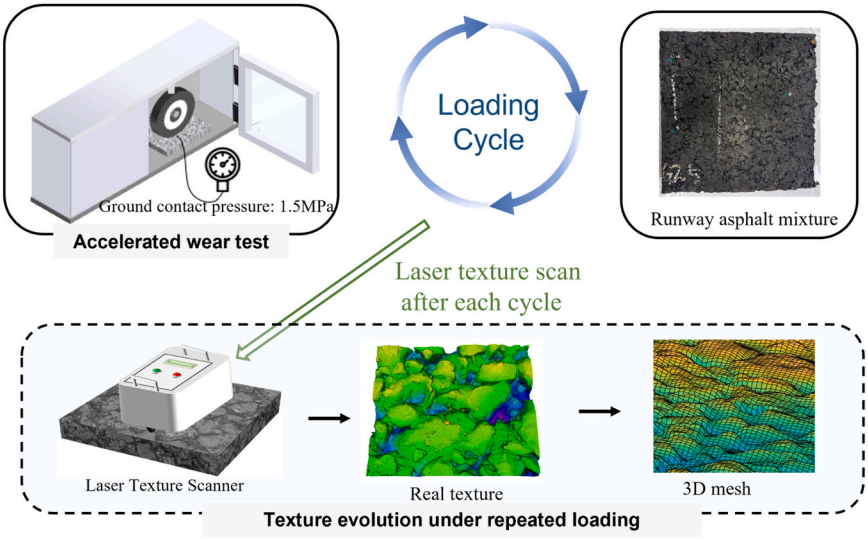

Fig. 2. Actual runway texture evolution and acquisition.

Table 4
Parameters of the equation of state for water.

Density ρ_0 (kg/m^3)	Viscosity (Pa·s)	Equation of State		
		c_0 (m/s)	s	Γ_0
998	$1*10^{-3}$	1480	1.97	0.11

per minute. The system also allows the test temperature and the total number of loading cycles to be preset according to the experimental requirements. After each wear stage, surface texture data were collected. To accurately capture the three-dimensional texture of the asphalt surface, a high-precision laser texture scanner (AMES 9400HD) was employed for data acquisition (as shown in Fig. 2). The laser texture scanner has an accuracy of up to 10 microns. A 40 mm × 40 mm test area was maintained throughout sequential wear cycles to ensure consistency. The detailed data acquisition procedure, including sampling interval, and surface preparation procedures, can be found in our previously published work [37]. The scanned data were then preprocessed through leveling and filtering to eliminate noise and improve accuracy. Finally, a custom MATLAB script was developed to convert the processed texture data into an ABAQUS-compatible inp file. This completed the modeling process from the measured three-dimensional texture data to the corresponding three-dimensional finite element mesh model. The process of texture acquisition is presented in the flowchart shown in Fig. 2.

2.3. Water film model

In this study, the Coupled Eulerian-Lagrangian (CEL) algorithm was employed to analyze hydroplaning behavior. The solid components (tire and runway) were modeled using Lagrangian elements, while the fluid (water) was modeled using Eulerian elements. The Volume of Fluid (VOF) method was used for free surface tracking, enabling visualization of the water-air interface by outputting the fluid volume fraction in the Eulerian mesh [42].

The pressure and density variations in the fluid were calculated using the Mie-Grüneisen equation of state for Newtonian fluids. The equation is given as follows [43]:

$$p = \frac{\rho_0 c_0^2 \eta}{(1 - s\eta)^2}\left(1 - \frac{\Gamma_0 \eta}{2}\right) + \Gamma_0 \rho_0 E_m \tag{2}$$

Where, p is hydrodynamic pressure; ρ_0 is the initial density of the water; η is dynamic viscosity, defined as $\eta = \rho_0/\rho$; ρ is the density of the water after being subjected to impact loading; $s = dU_s/U_p$ is Hugoniot slope coefficient, U_s is shock wave velocity, U_p is particle velocity, follow the linear Hugoniot relation: $U_s = c_0 + sU_p$. Γ_0 is the initial value of the material parameter, c_0 is the speed of sound in the fluid.

To define the water flow state in ABAQUS, curve fitting was performed using real experimental data on the impact behaviour of water [43]. The material parameters for water are summarized in Table 4.

In this study, a fluid flow model was adopted, and the tire motion was simulated using a relative coordinate transformation approach. The tire model possessed only rotational degrees of freedom, while its horizontal translation was fully constrained. A prescribed angular velocity corresponding to the target rolling condition was applied to the tire. Both the runway and the water in the Eulerian domain were assigned a uniform horizontal velocity equal to the aircraft forward speed in the global coordinate system [35]. This setup provides the tire with an effective relative velocity identical to that in the actual forward-travel scenario. The Eulerian domain was set to dimensions of 1000 mm × 420 mm × 200 mm, fully covering the contact area between the tire tread and runway, thereby ensuring numerical stability and computational accuracy.

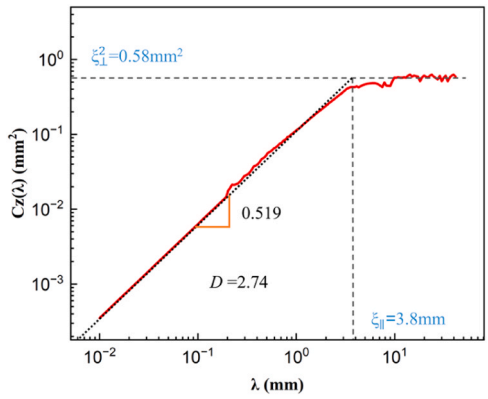

Fig. 3. Height-difference autocorrelation function curve.

2.4. Interaction model

The friction between a tire and the runway can be decomposed into two fundamental components: the adhesive friction component and the hysteresis friction component. The adhesive component arises from molecular interactions between the rubber tire and the runway surface during the sliding process. In contrast, the hysteresis component is associated with energy dissipation resulting from tire deformation during the sliding process. The latter is strongly influenced by runway surface texture, particularly under wet and rough surface conditions, where it becomes a critical factor governing tire-runway skid resistance. In this study, the Kluppel-Heinrich friction model is introduced to characterize the interaction between the rubber tire surface and the runway. The solution procedure for this model comprises three main stages:

(i) Spectral processing of runway texture features. High-resolution three-dimensional runway texture data were first acquired using a precision laser texture scanner. The height-difference autocorrelation function was then applied to transform the measured texture data into the frequency domain, thereby extracting the dominant characteristics of surface roughness. This process is described using three key parameters: the Hurst exponent H (related to the fractal dimension D), the horizontal correlation length $\xi_\parallel$, and the vertical correlation length $\xi_\perp$ [44]. Fig. 3 illustrates the height-difference autocorrelation function curve corresponding to the measured texture.

Accordingly, the runway texture can be characterized using the following PSD function [45]:

$$S(\omega) = \frac{H\xi_\perp^2}{2\pi v_{eq}\xi_\parallel}\left(\frac{\omega}{\omega_{\min}}\right)^{-(2H+1)} \tag{3}$$

Where, ω is defined as the angular frequency, it is related to the texture wavelength λ, $\omega = 2\pi v_{eq}/\lambda$. $\omega_{\min}$ denotes the minimum angular frequency, corresponding to the maximum characteristic texture wavelength. v_{eq} is retained to denote the equivalent sliding velocity used in the theoretical formulation for mapping the spatial pavement texture into the frequency domain.

(ii) Modeling of rubber viscoelastic properties. The viscoelastic behavior of the rubber material was characterized using the Zener model [46].

(iii) Friction coefficient calculation. The contact conditions between the tire tread rubber and the runway texture were simulated based on the Greenwood-Williamson contact model. By quantifying the energy dissipation induced by rubber hysteresis deformation and applying the principle of energy conservation, the analytical expression for the hysteresis friction coefficient was derived [45]:

$$\mu_{HK} = \frac{\langle z_p \rangle}{8\pi^2 \sigma_0 v_s}\int_{\omega_{\min}}^{\omega_{\max}} \omega E''(\omega)\mathrm{PSD}(\omega)d\omega \tag{4}$$

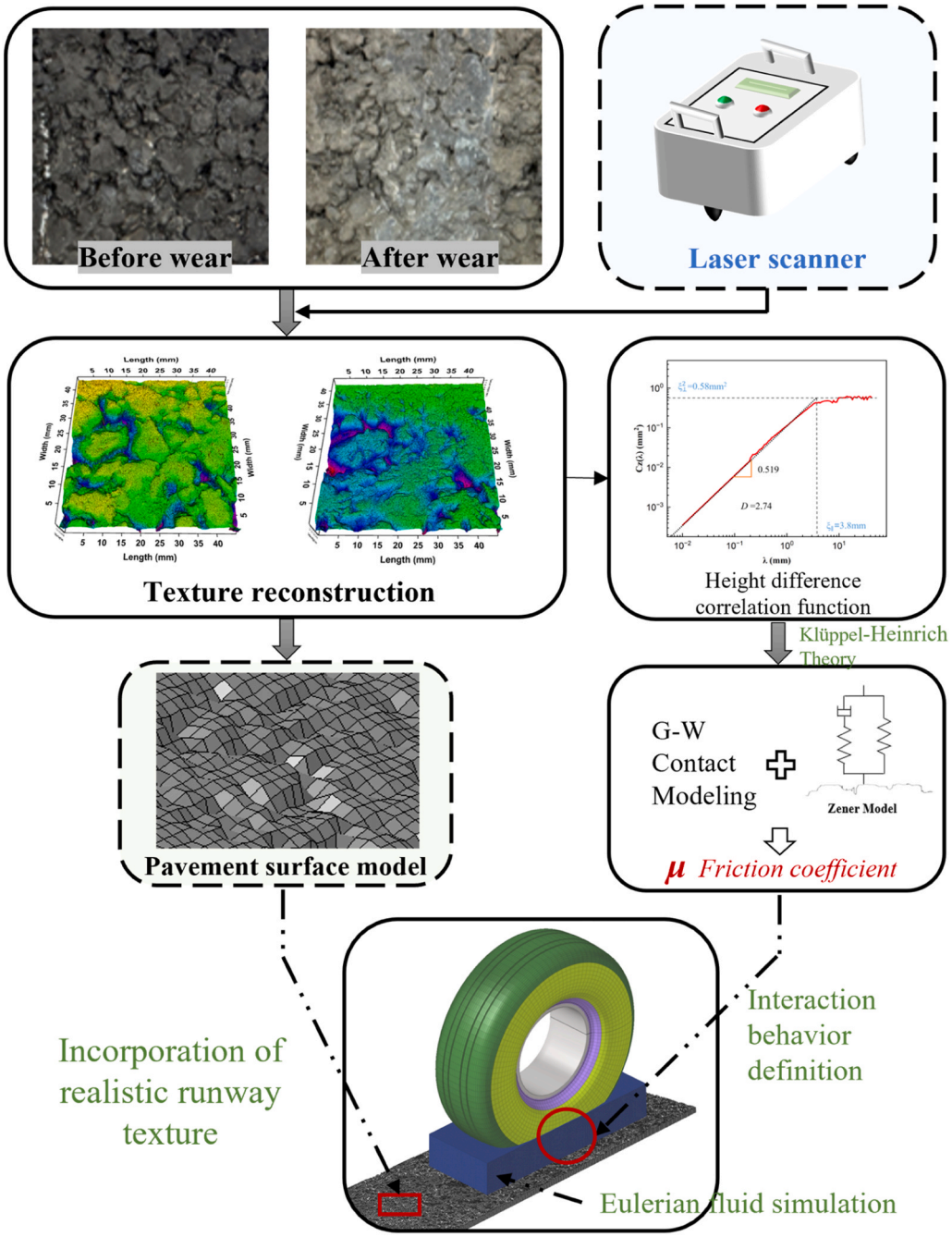

Fig. 4. Modeling workflow of the tire-runway-fluid coupled model.

Where, $\langle z_p \rangle$ denotes the mean deformation amplitude of the rubber contact surface; σ_0 is the average normal stress within the contact region; ω_{max}, ω_{min}: upper and lower integration limits, corresponding to the maximum and minimum characteristic wavelengths of the pavement texture, respectively; v_s is sliding velocity.

Fig. 4 presents the overall finite element modelling workflow for the tire-runway-fluid interaction adopted in this study.

2.5. Analysis of skid resistance and braking distance

2.5.1. Skid number evaluation

Regarding the model output, during hydroplaning, the tire is subjected to various vertical forces, including axle load, ground reaction force, and fluid-induced lift. In the horizontal direction, the tire

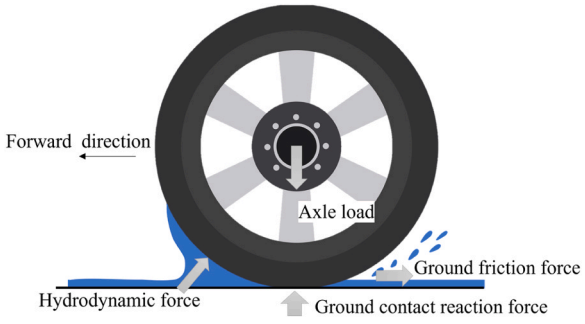

Fig. 5. Schematic diagram of the forces acting on the tire during hydroplaning.

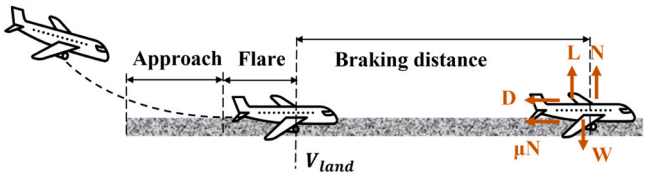

Fig. 6. Schematic diagram of aircraft landing and corresponding force analysis diagram.

experiences complex interactions, such as frictional resistance between the runway and rubber, as well as hydrodynamic impact from water flow (as illustrated in Fig. 5).

The skid number (SN) is used to characterize the skid resistance of the tire during motion on the runway, as defined in Eq. [5] [25]:

$$SN = \frac{F}{F_z} \times 100 \tag{5}$$

Where $SN = 100\mu$, μ is the friction coefficient, F_z is vertical load, F is the total frictional force in the tire-runway contact area [25,47], obtained directly from the coupled simulation.

2.5.2. Braking distance prediction

The skid-resistance simulation model developed in this study is designed to replicate the dynamic behavior of aircraft tires during the braking phase. The model enables the prediction of tire skid-resistance performance under varying conditions, including speed, load, runway characteristics, and water film thickness, thereby providing theoretical support for safety assessments under wet runway conditions.

The aircraft landing process can be divided into three stages: the approach phase, the flare phase, and the braking phase (as shown in Fig. 6). The braking distance S is defined as the ground roll distance from the initiation of braking until the aircraft comes to a complete stop or exits the runway, and is obtained by integrating the velocity over this period.

$$S = \int_0^T v(t)dt \tag{6}$$

Where, $v(t)$ represents the instantaneous velocity during braking, and T denotes the braking duration.

In the calculations, it is assumed that the aircraft does not employ reverse thrust and that the runway is level. Under these conditions, the longitudinal motion of the aircraft on the runway can be expressed as:

$$\mathrm{D} + \mu \mathrm{N} = Ma_b \tag{7}$$

Where, a_b is the braking acceleration, M is the aircraft mass, μ is the runway friction coefficient, and N is the normal force acting on the tire. Considering the effect of wing lift, the normal force can be expressed as $N = Mg - L$. The lift and aerodynamic drag are calculated as:

$$L = 0.5\rho_a v^2 A_{ref} C_L, \quad D = 0.5\rho v^2 A_{ref} C_D \tag{8}$$

where ρ_a is the air density, A_{ref} is the reference wing area, and C_L and C_D are the lift and drag coefficients, respectively. Accordingly, the final expression for the braking distance S is obtained according to Ref. [25]:

$$S = \int_0^T \left[V_{land} - \left([\mu(t)]g + \frac{0.5\rho[v(t)]^2 A_{ref}(C_D - [\mu(t)]C_L)}{M} \right) t \right] dt \tag{9}$$

Where, V_{land} is the landing speed of the aircraft.

This calculation process not only accounts for the contribution of tire-runway friction, but also incorporates the reduction of normal force caused by aerodynamic lift, as well as the influence of aerodynamic drag. Such treatment enables a more accurate characterization of the braking dynamics and provides a conservative estimate of the actual braking distance.

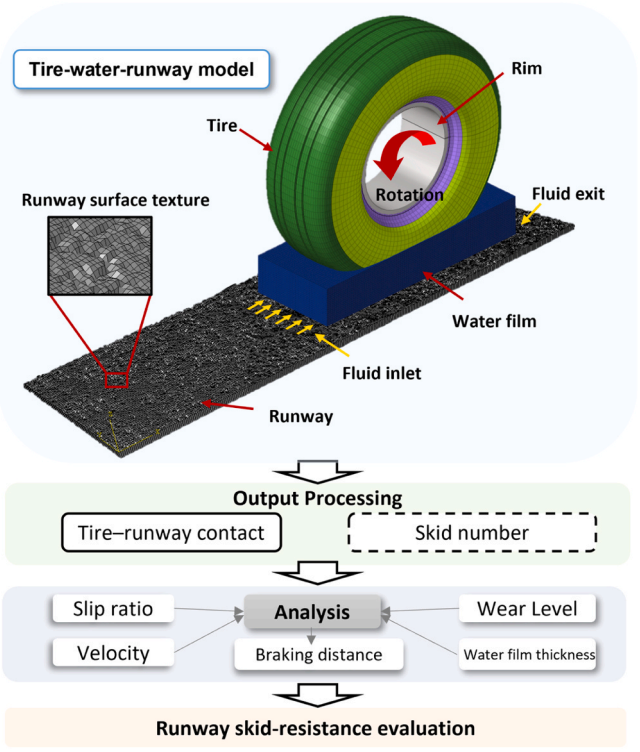

Fig. 7. Skid resistance evaluation framework.

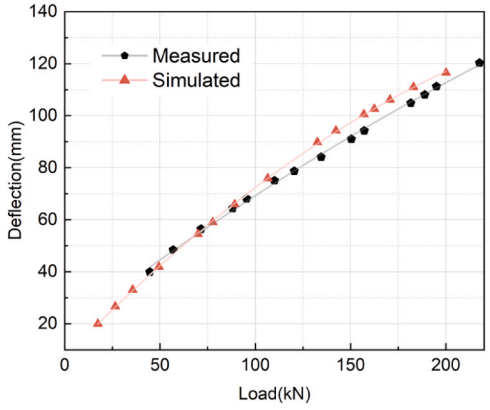

Fig. 8. Tire stiffness validation curve.

Following the development of the tire-runway-fluid coupled model, comprehensive post-processing and analysis were conducted. Based on simulation results under varying operational conditions, this study systematically investigates the patterns of variation in runway skid resistance. This effort culminates in an experimental-numerical integrated framework for skid-resistance safety evaluation, the workflow of which is illustrated in Fig. 7.

3. Model validation

In the 1980s, Tielking conducted static vertical loading tests on a 49 × 17 aircraft tire, systematically measuring the relationship between radial stiffness and deflection under different loads [38]. To validate the accuracy of the finite element tire model developed in this study, a static loading simulation was carried out under the same tire size and loading conditions. The resulting load-deflection curve obtained from numerical simulation was compared with the experimental results, as shown in

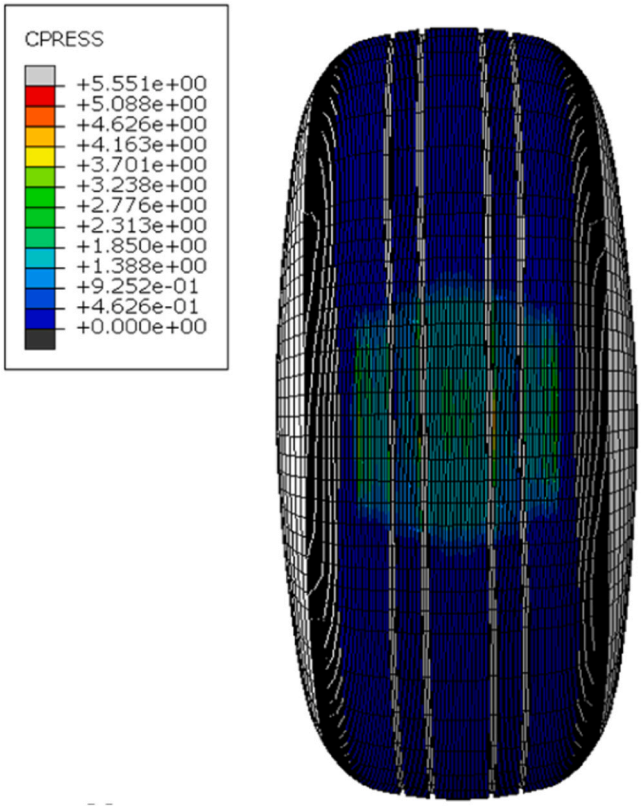

Fig. 9. Tire contact footprint diagram.

Table 5
Experimental and simulated footprint values.

Load (kN)	Tire footprint length			Tire footprint width		
	Measured (mm)	Simulated (mm)	Error (%)	Measured (mm)	Simulated (mm)	Error (%)
106.8	393.7	396.2	0.64	247.7	250.1	0.97
160.1	467.8	474.6	1.45	279.3	282.7	1.22
200.1	528.6	537.4	1.66	307	313.9	2.25

Fig. 8. The results indicate a good agreement between the measured and simulated deflections. This agreement demonstrates that the model's settings for tire geometry, material properties, and initial inflation pressure can realistically capture the tire's deformation behavior, providing a reliable basis for subsequent tire-runway interaction simulations.

To further evaluate its contact characteristics, a contact patch validation was performed. The simulated tire contact footprint is shown in Fig. 9.

Under an inflation pressure of 1.31 MPa, the numerical contact patches were obtained for various test loads. These results were compared with the experimental measurements, as presented in Table 5 [25]. The inflation pressure was set at 1.31 MPa. The results show that the simulated contact areas closely match the measured values, with relative errors within 4 % for all conditions. This further confirms the applicability and accuracy of the model for subsequent condition analyses.

Furthermore, to assess the applicability of the developed tire-runway-fluid coupled model under wet conditions, it is necessary to validate the aircraft tire hydroplaning model. Under hydroplaning conditions, the interaction between the tire, the water film, and the runway surface becomes more complex, and accurately capturing this interaction is essential for predicting skid resistance and ensuring reliable safety assessments. In this study, an ungrooved asphalt concrete pavement surface consistent with the pavement type used in the FAA experiments was selected. The test conditions were set according to typical FAA hydroplaning experiments, with a water film thickness of 0.25 mm and a vertical load of 156 kN. Skid numbers were computed at different speeds and compared with the experimental hydroplaning results conducted by the FAA [48], as shown in Fig. 10(a). The simulated and experimental friction coefficients for the flooded and puddled conditions are also compared, as presented in Fig. 10(b). The results show that the skid resistance values obtained from the numerical simulation are in good agreement with the experimental results in both overall trend and magnitude. This confirms that the aircraft tire hydroplaning model developed in this study can effectively represent hydroplaning behaviour.

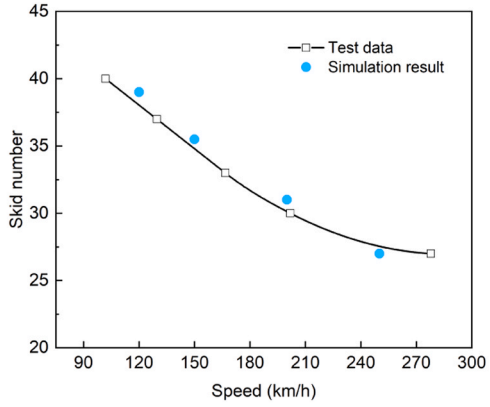

(a) Comparison of simulated and experimental skid numbers at different speeds.

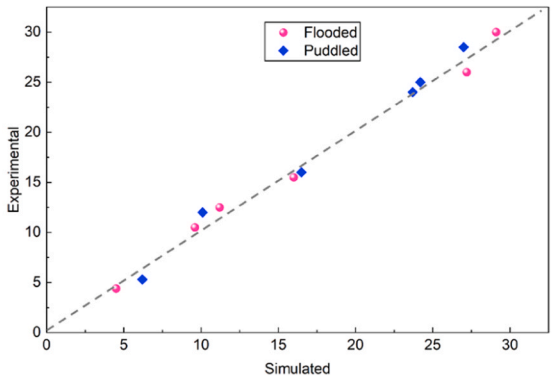

(b) Comparison between simulated and experimental friction coefficients under flooded and puddled conditions

Fig. 10. Friction coefficient validation curve.

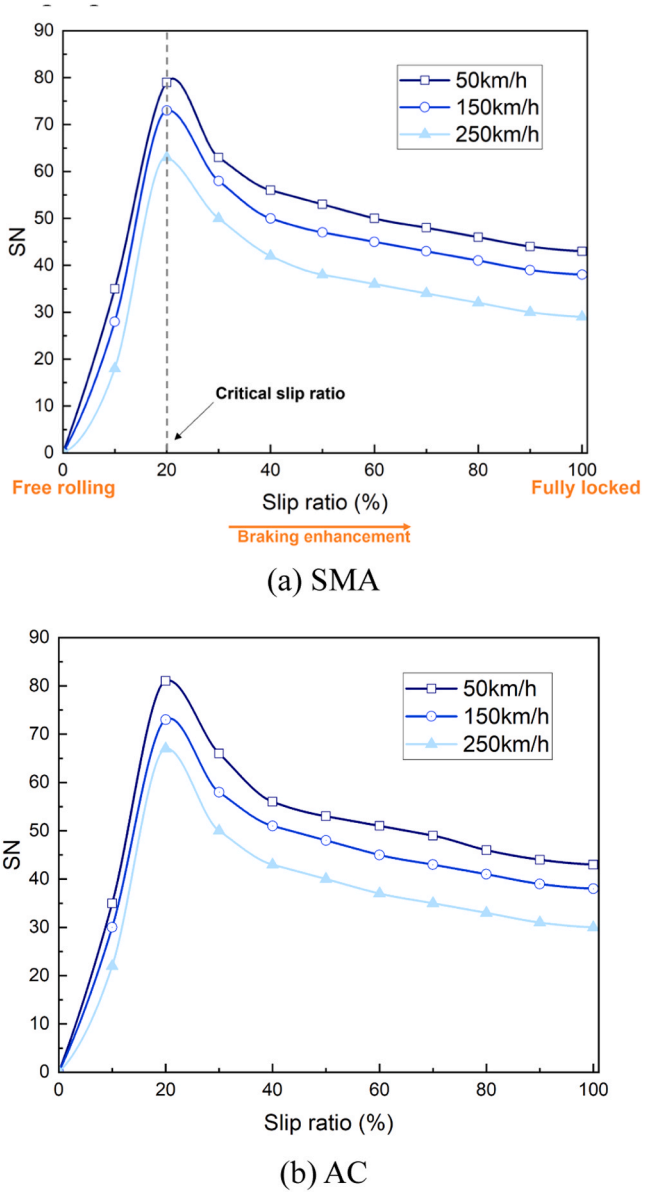

Fig. 11. Relationship between runway skid number and slip ratio at different speeds (inflation pressure: 1.5 MPa, load: 156 kN, state: dry).

4. Results and discussion

4.1. Effects of slip ratio on skid number

Aircraft tires are typically equipped with anti-lock braking systems (ABS) to maintain the slip ratio within an optimal range during braking, thereby maximizing braking force. The tire slip ratio (SR) is a key parameter for characterizing longitudinal tire slip and is defined by Eq. [10] [25]:

$$Slip\ Ratio = \frac{V - V_{tire}}{V} \times 100 = \frac{V - \omega_t R}{V} \times 100 \quad (10)$$

Where V is the aircraft's forward velocity, ω_t is the angular velocity of the tire, and R is the effective rolling radius of the tire. A slip ratio of 0 % indicates pure rolling, while a slip ratio of 100 % represents fully locked.

In this study, skid resistance was analyzed on two types of asphalt pavement gradations under three aircraft speeds: low (50 km/h), medium (150 km/h), and high (250 km/h). Fig. 11 presents the variation of skid number (SN) with different slip ratios for both pavements.

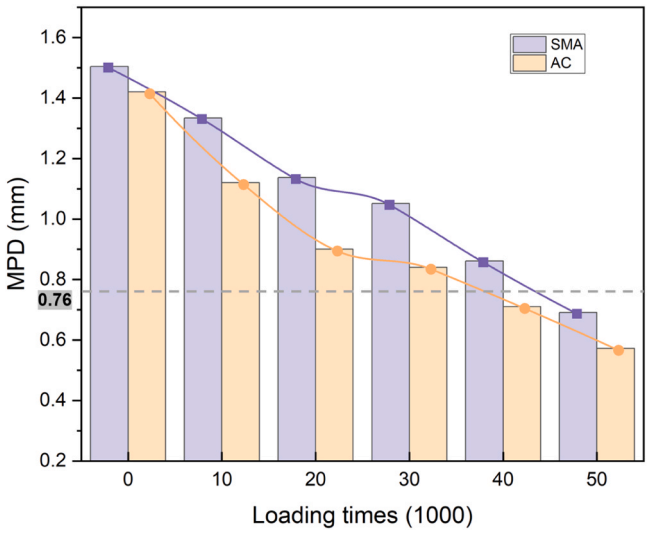

Fig. 12. MPD of the asphalt mixture surface.

The results show that the skid number changes significantly with the slip ratio. Specifically, in the initial stage (0 %-20 %), SN increases rapidly with slip ratio and reaches a peak at around 20 %, referred to as the critical slip ratio. Beyond this point, SN gradually decreases. This critical slip ratio aligns well with the optimal slip ratio range (about 20 %) reported in existing literature [48], further validating the accuracy of the proposed model.

The data in Fig. 11 also indicate that increasing aircraft speed mainly results in lower SN values in the high-slip-ratio range (>20 %). At a high speed of 250 km/h, the SN level remains consistently lower than that at 50 km/h and 150 km/h once the slip ratio exceeds the optimal range. This suggests that as speed increases, the entire SN curve shifts downward, reducing the overall friction capacity. Accordingly, accurate ABS control is required, as even a slight deviation from the optimal slip ratio results in a markedly diminished braking reserve, which is consistent with the findings reported in Ref. [35].

4.2. Effects of wear on skid number

Fig. 12 illustrates the variation in Mean Profile Depth (MPD) of the asphalt mixture pavement under different numbers of loading cycles. As the number of load applications increases, the macro-texture depth of the pavement shows a continuous decreasing trend.

Under the assumed optimal slip ratio of 20 %, the skid resistance of both pavement types was evaluated, as shown in Fig. 13. Overall, the skid number (SN) for both surfaces decreases significantly as wear increases. In addition, the final worn state exhibits the lowest SN value across all tested speeds.

For the SMA surface, a sharp reduction in SN is observed when the loading cycles reach 50,000. In the case of the AC surface, a notable decline begins after 40,000 cycles. As shown in Fig. 12, the MPD for both pavements drop below 0.76 mm under these wear conditions. According to the findings of reference [49], when the macro-texture depth falls below 0.76 mm, a significant reduction in skid resistance is expected. This observation aligns well with the simulation results obtained in this study.

In addition, it can be clearly observed that under all loading conditions, the SMA pavement consistently exhibits higher skid numbers than the AC pavement, indicating its superior skid resistance and durability. This trend is also reflected in the MPD data, as the SMA surface maintains a greater macro-texture depth.

The fundamental reason for this performance difference lies in the gradation characteristics of the two asphalt mixtures. SMA utilizes a higher proportion of coarse aggregates, forming a stable coarse

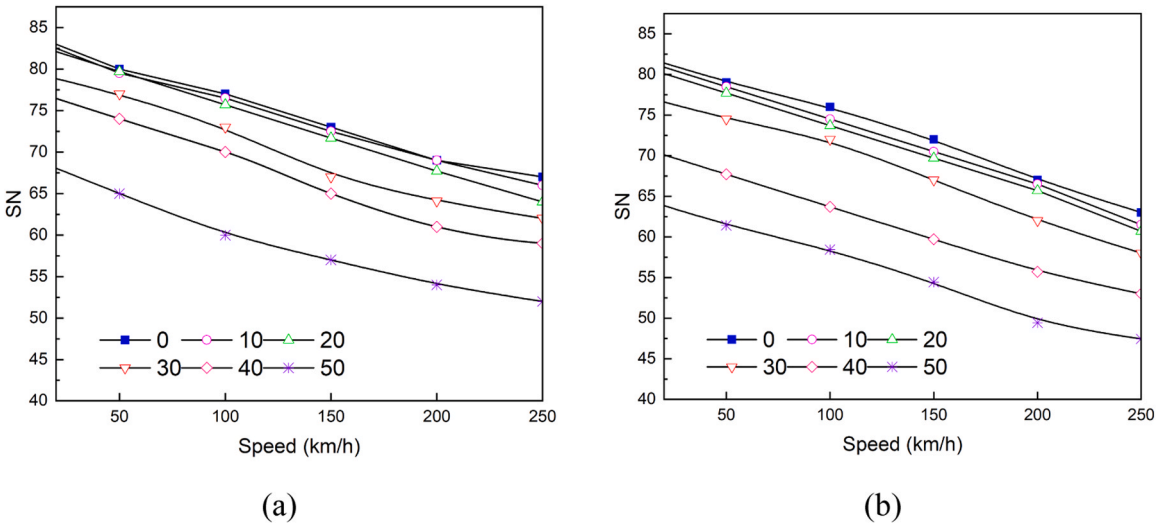

Fig. 13. SN at different wearing cycles for (a) SMA, (b) AC (inflation pressure: 1.5 MPa, load: 156 kN, state: dry, SR: 20 %).

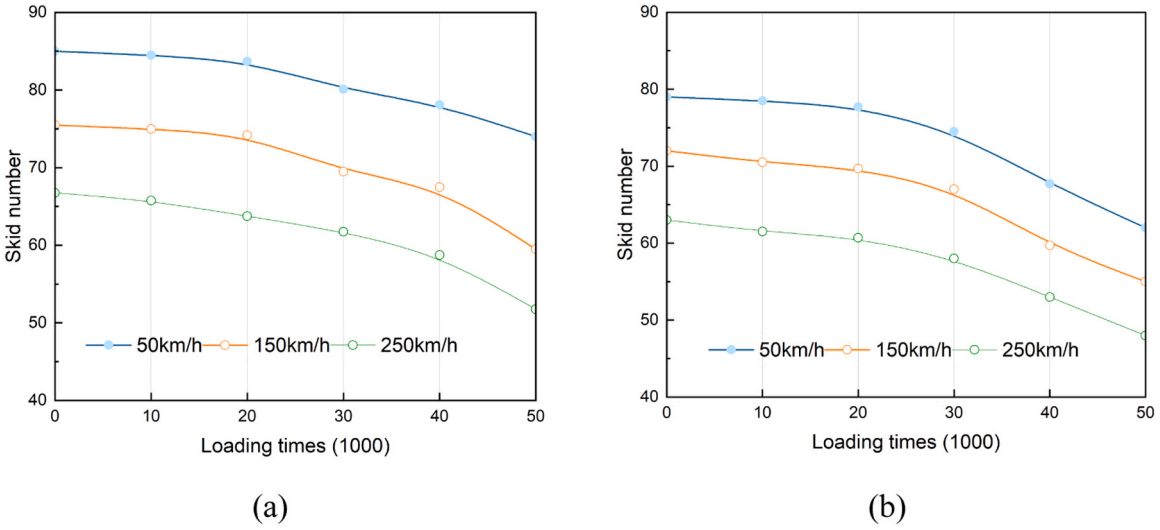

Fig. 14. SN at different speeds for (a)SMA, (b) AC (inflation pressure: 1.5 MPa, load: 156 kN, state: dry, SR: 20 %).

aggregate skeleton, which results in a more pronounced macro-texture structure [50]. This enhanced surface texture increases the effective frictional interface between the tire and runway, enlarges the actual contact area, and consequently improves skid resistance.

Therefore, from the perspective of optimizing airport runway material selection and design, SMA-type mixtures with higher coarse aggregate content should be prioritized. This approach can significantly improve skid resistance, extend runway service life, and enhance operational safety during aircraft landing and braking.

4.3. Effects of velocity on skid number

As shown in Fig. 14, skid resistance exhibits a clear downward trend with increasing aircraft speed under the same wear level. This observation indicates that speed has a significant impact on skid performance.

Specifically, in Fig. 14(a), as the aircraft speed increases from 50 km/h to 250 km/h, the skid number decreases significantly across all wear stages. For example, at 20,000 loading cycles, the skid number at 250 km/h is approximately 23.5 % lower than that at 50 km/h. Moreover, this decreasing trend becomes more pronounced as surface wear intensifies. At 50,000 loading cycles, the reduction in skid resistance under high-speed conditions reaches approximately 31 %.

As the tire speed increases, the excitation frequency induced by the pavement macro-texture becomes higher, shifting the rubber response into a high-frequency regime where the loss modulus decreases. The reduced viscoelastic energy dissipation weakens the hysteresis friction component, which is governed by the loss modulus, resulting in a lower effective friction force at the tire-runway interface.

Therefore, during runway service, it is essential to monitor macro-texture characteristics and evaluate their corresponding skid resistance regularly. In summary, both vehicle speed and macro-texture depth play critical roles in influencing skid resistance, in agreement with previous findings reported in Ref. [49].

4.4. Effects of water film depth on skid number

The developed tire-water-runway interaction model was used to compute the tire-runway contact forces within the effective contact area, taking into account the fluid intrusion effect. Fig. 15 presents the bottom view, top view, and side view of the aircraft tire footprint during hydroplaning, as simulated by the finite element model under a water film thickness of 3 mm and a speed of 150 km/h. The water flow

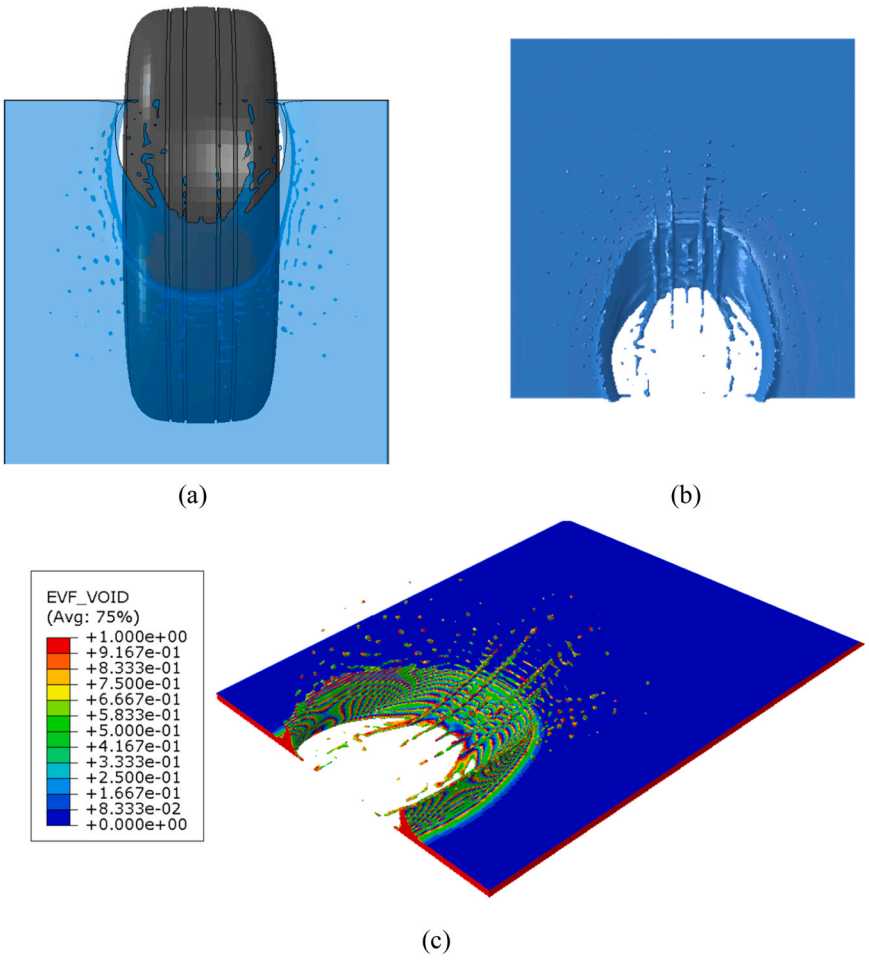

Fig. 15. Aircraft tire footprint during hydroplaning obtained from FE simulation: (a) bottom view, (b) top view, and (c) side view.

channels are visualized using the Eulerian Volume Fraction (EVF), which represents the fluid occupancy within the computational domain.

Fig. 16 presents the simulated skid number (SN) results for two asphalt mixtures before and after loading, under three typical water film thicknesses (1 mm, 3 mm, and 5 mm), as a function of aircraft speed. Due to the presence of small viscous and hydrodynamic drag forces, the friction coefficient at the tire-runway interface does not drop to zero even during hydroplaning. Therefore, as reported by the FAA, the aircraft is considered to have reached its dynamic hydroplaning state when the skid number decreases to SN = 5.0 [48,51]. Accordingly, this study identifies the critical hydroplaning velocity for each water-film thickness as the vehicle speed at which SN drops to 5.

4.4.1. Variation of skid number with water film depth

Based on this assumption, the results show that under partially flooded conditions (i.e., partial hydroplaning), the skid number decreases significantly with increasing water film thickness. Moreover, the SN reduction becomes progressively larger as the water depth increases. Taking the loaded SMA runway as an example, when the vehicle speed was 50 km/h, the skid resistance decreased by 6.5 %, 14.3 %, and 24.7 % at water film thicknesses of 1 mm, 3 mm, and 5 mm, respectively, compared to the dry condition (0 mm water film). When the speed increased to 250 km/h, the skid resistance reductions under the same water film thicknesses rose to 17.9 %, 47.8 %, and 74.6 %, respectively. This highlights the significant weakening effect of water films on skid resistance at high speeds.

In addition, comparison before and after abrasion shows that the skid number (SN) of both asphalt mixtures decreases significantly after 20,000 loading-abrasion cycles. After abrasion, the skid resistance of the SMA pavement remains consistently higher than that of the AC pavement. As further illustrated in Fig. 17, under identical water-film thicknesses and abrasion conditions, the critical hydroplaning speed of the SMA pavement is generally higher than that of the AC pavement. This indicates that the degradation of macrotexture plays a decisive role in controlling wet-surface skid resistance.

As shown in Fig. 16(d), the light blue shaded region represents the Sensitive Water Depth Range. Most of the total SN reduction within the 0–5 mm water film depth occurs in the 1–5 mm interval. For example, at a speed of 200 km/h, 72.4 % of the total SN reduction from 0 to 5 mm is contributed by the change occurring between 1 and 5 mm. This suggests that even slight variations in water film thickness can result in significant fluctuations in the skid number. This highlights the need for careful monitoring and control of water film thickness within this sensitive range during actual pavement maintenance-particularly under high-speed rolling conditions.

Fig. 18 illustrates the variation in skid resistance of the SMA pavement (after 20,000 loading cycles) with aircraft speed and water film thickness. The results clearly show that SN decreases markedly as both speed and water depth increase. This further confirms the strong coupling effect between speed and water film thickness on skid resistance. The combined occurrence of high speed and thick water film leads to a pronounced degradation in pavement friction performance. Therefore, in airport runway operations and maintenance, special attention should be given to the interaction between aircraft speed and surface water accumulation.

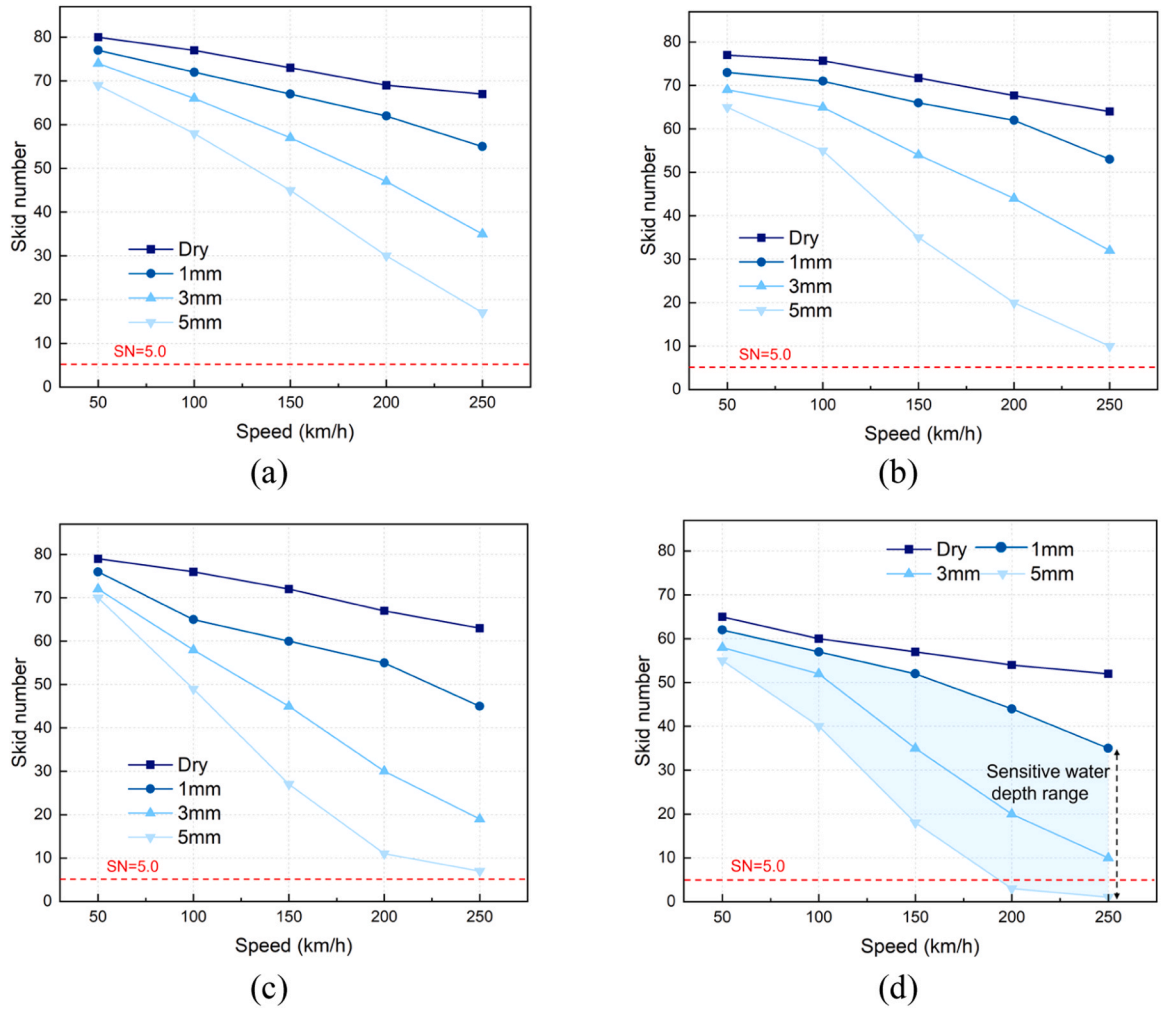

Fig. 16. SN under different water film thicknesses (a) SMA-before wear, (b) SMA-after wear, (c) AC-before wear, (d) AC-after wear.

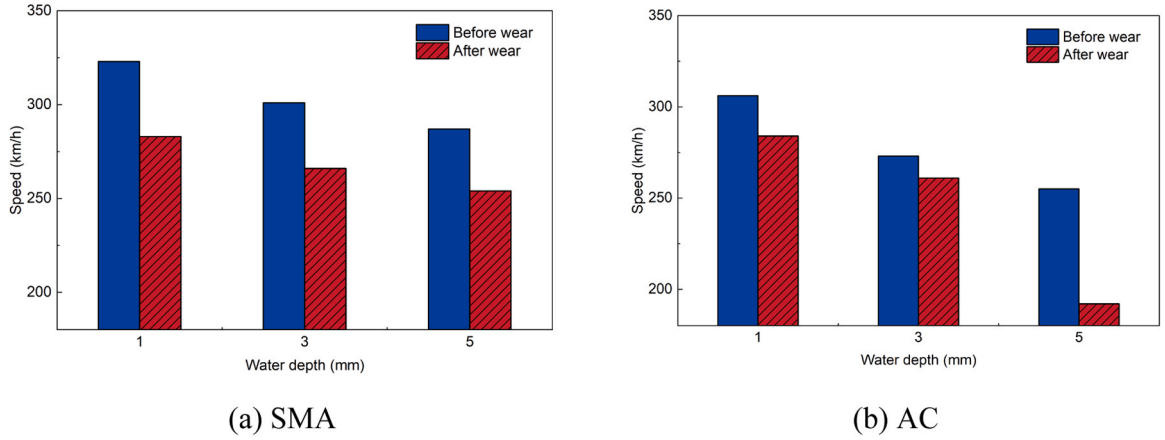

Fig. 17. Hydroplaning velocities of asphalt mixtures.

4.4.2. Mechanism of skid resistance degradation based on tire-pavement contact evolution

To further clarify the mechanisms underlying the variation in skid resistance, this section analyzes the tire-pavement contact state during hydroplaning. The analysis is based on the schematic "three-zone" hydroplaning model (Fig. 19) and the evolution of tire-pavement contact forces (Fig. 20).

Tire hydroplaning is a complex phenomenon. It involves the coupled effects of tire deformation, transient fluid flow, and pavement texture. Previous studies have shown that the "three-zone" model can effectively describe the contact relationship among the tire, water, and pavement during hydroplaning. According to the contact condition, the hydroplaning interface can be divided into three typical zones: the submerged zone (Zone I), the transition zone (Zone II), and the contact zone (Zone

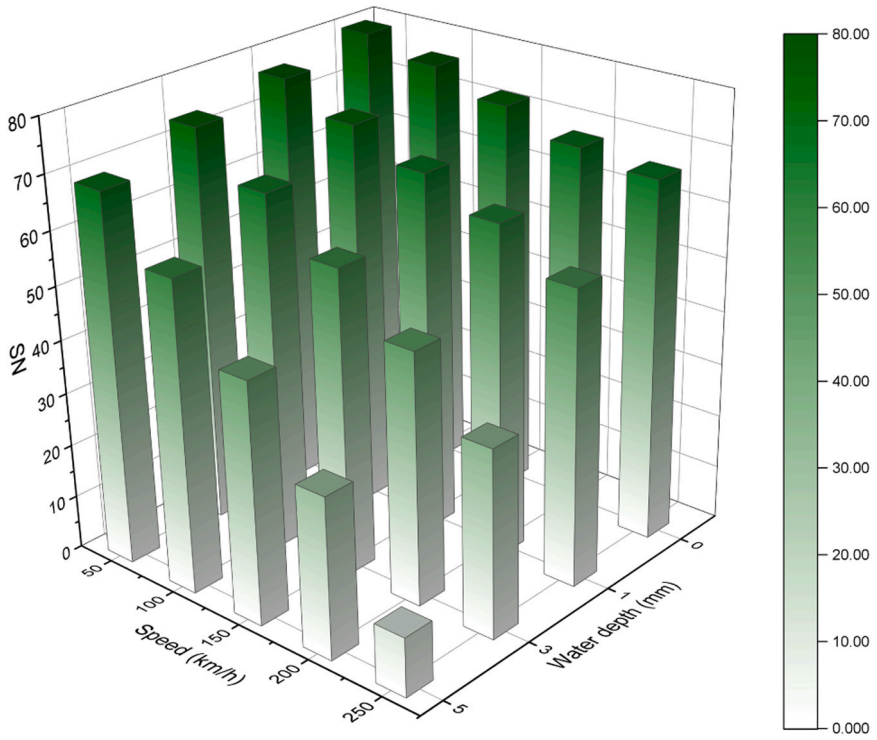

Fig. 18. SN under different speeds and water film thicknesses.

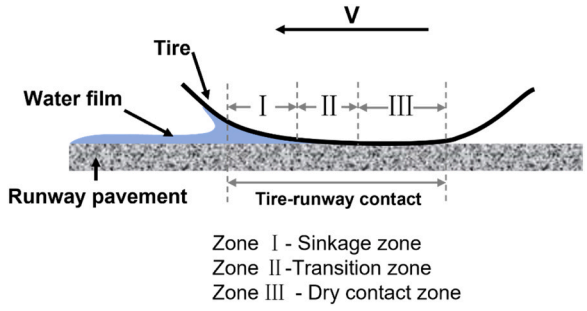

Fig. 19. Three-zone diagram of hydroplaning behavior.

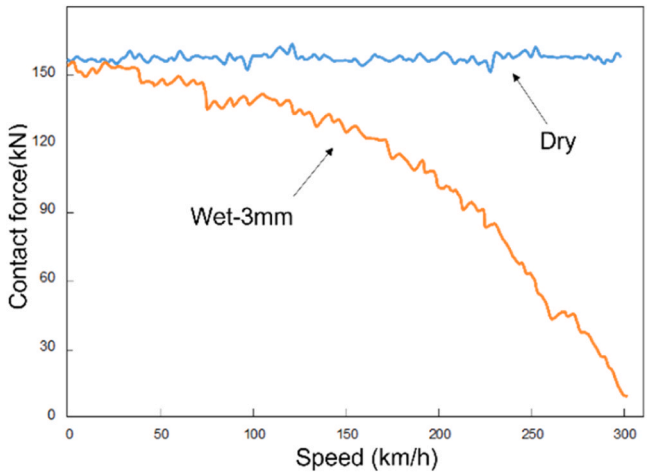

Fig. 20. Variation of vertical contact force on dry and wet pavements.

III) (Fig. 19). The distribution of these three zones changes with vehicle speed. At low vehicle speeds, the contact zone (Zone III) dominates, and surface water can be effectively expelled through tire grooves and pavement macrotexture. Under such conditions, a large real contact area is maintained between the tire and pavement, enabling sufficient traction to be provided. As the vehicle speed increases, Zones I and II gradually expand along the contact patch. At the same time, the area of Zone III continuously decreases. When the sinkage zone nearly covers the entire contact area, the tire becomes completely separated from the pavement surface and enters a fully developed state of dynamic hydroplaning. The corresponding vehicle speed at this moment is also defined as the critical hydroplaning speed.

The nonlinear decrease in SN with increasing speed, as shown in Fig. 16, reflects the dynamic migration of the three hydroplaning zones across the tire-pavement contact area. Fig. 20 presents the numerical simulation results of the vertical contact force acting on the tire as a function of vehicle speed under dry conditions and with a water film thickness of 3 mm. Due to structural damping and vibration during tire motion, local oscillations appear in the force response. Under dry conditions, the vertical tire-pavement contact force remains nearly constant over the entire speed range. This indicates that the pavement almost entirely supports the vertical load, ensuring stable contact between the tire and the pavement surface.

In contrast, under wet conditions, the actual vertical contact force continuously decreases with increasing speed. This reduction is primarily attributed to the strong compression of the water film at the tire leading edge as the vehicle speed increases, which leads to a continuous rise in hydrodynamic pressure. The resulting hydrodynamic lift acting on the tire is therefore progressively enhanced and gradually offsets the vertical supporting force provided by the pavement, causing a continuous reduction in the real contact area between the tire and the pavement. When the hydrodynamic lift becomes nearly balanced with the external vertical load, the tire is almost completely supported by the water film, and the effective support from the pavement approaches zero. At this stage, the tire enters a fully developed state of dynamic hydroplaning. From the perspective of contact mechanics, this process

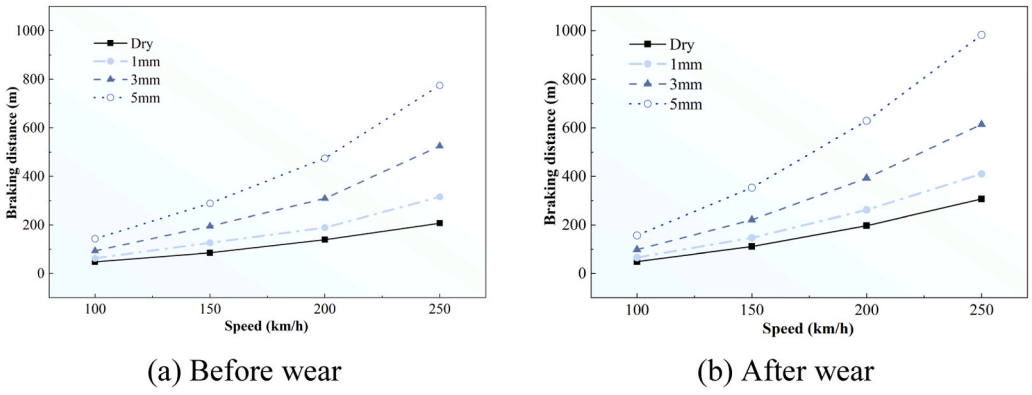

Fig. 21. Braking distance before and after Wear.

explains the fundamental mechanism responsible for the sharp deterioration of skid resistance at high speeds under wet conditions.

4.5. Braking distance

Fig. 21 shows the braking distances before and after pavement wear under different water film thicknesses. It can be observed that, both before and after wear data show a significant increase in braking distance with rising speed. In terms of water film, the thickness of the water film has a significant influence on braking performance. The thicker the water film, the longer the braking distance. Differences are more minor at lower speeds but become much larger at higher speeds. When the water film thickness reaches 5 mm, the braking distance approaches 1 km (Fig. 21(b)), indicating that the combined effects of water film and speed can significantly amplify braking risk.

Comparing before and after wear conditions under wet surfaces, after-wear braking distance curve is noticeably steeper, meaning that braking distance becomes more sensitive to changes in speed. This suggests that as the surface macrotexture depth decreases, the influence of vehicle speed on the required braking distance becomes more pronounced. The primary reason is that reduced macrotexture significantly weakens drainage capacity. Consequently, for the same external water film thickness, the residual water film between the tire and runway is greater after wear.

From a hydrodynamic perspective, a smaller macrotexture cannot effectively expel water. Hydrodynamic pressure builds up faster within the contact area, sometimes leading to localized partial hydroplaning. This results in a lower critical hydroplaning speed, reduced available friction, and significantly increased braking distances under the same water film and braking conditions. The effect is particularly pronounced when thick water films and high speeds occur together, creating a triple amplification effect from speed, water film, and texture loss.

Therefore, wear not only reduces the friction coefficient but also magnifies the combined effects of water film and speed. These findings highlight the importance of maintaining adequate macrotexture depth on airport runways to limit braking distance growth and delay the onset of hydroplaning.

5. Conclusions

This study developed an improved finite element model that incorporates the coupled interactions among tire, runway, and fluid. A comprehensive evaluation method for skid resistance was proposed by integrating laboratory experiments with numerical simulations. This approach accurately simulates the degradation process of wet-runway skid resistance by coupling actual worn texture data with numerical simulations. In the model, sequentially worn runway textures obtained via laser scanning were directly incorporated as geometric boundary inputs. Furthermore, the friction model parameters were calibrated based on experimental results, allowing for a more accurate representation of the progressive deterioration in skid resistance performance. Based on this model, the interactions between tire, runway, and fluid were analyzed under various operating conditions, revealing the variation patterns in skid resistance across different scenarios. Key conclusions are summarized as follows:

1. Skid resistance decreases with runway surface wear. A strong correlation was observed between the reduction in surface texture depth and degradation of skid resistance. Continuous monitoring of runway texture throughout its service life is essential to ensure surface safety performance.

2. SMA mixtures demonstrated superior skid resistance compared to AC mixtures. Under the same loading cycles and speed conditions, SMA pavements sustained skid number approximately 10 % higher than AC pavements, indicating better macro-texture retention and wear resistance. SMA graded mixtures with a higher coarse aggregate content are recommended for airport pavements to ensure long-term skid resistance.

3. Aircraft speed has a significant impact on skid resistance. As speed increases, the skid number decreases steadily due to reduced friction between the tire and the runway. The skid resistance of the asphalt mixture decreased by 31 % as the aircraft speed increased from 50 km/h to 250 km/h.

4. Water film thickness substantially impacts skid resistance. When the water film thickness increased from 0 mm (dry) to 5 mm, the skid number decreased by up to 25 % at 50 km/h. At 250 km/h, the reduction reached approximately 70 %, indicating a heightened risk of hydroplaning. The combined effect of high speed and thick water film is a key factor contributing to dynamic hydroplaning. Therefore, joint monitoring of aircraft speed and surface water depth is crucial for runway safety management.

5. Braking distance increases significantly with both speed and water-film thickness. Maintaining adequate pavement macrotexture and drainage capacity is crucial for mitigating the increase in braking distance under wet conditions and ensuring safe landings.

It should be emphasized that the present model does not incorporate a temperature field. Since rubber friction is known to decrease with increasing temperature, omitting the thermal effect may lead to friction predictions that are not fully conservative, especially under high-speed or long-duration operating conditions. This simplification was made to ensure computational efficiency, as the primary focus of this study is the macroscopic interaction among the aircraft tire, pavement texture, and the interfacial fluid film. Future work will incorporate thermo-mechanical coupling into the tire-pavement-fluid model, enabling a more realistic representation of friction evolution and improving the applicability of the model for engineering design and safety evaluation.

Statement of originality

We hereby affirm that the manuscript titled " Skid Resistance

Assessment of Wet Asphalt Runways by Coupling Finite Element Simulation with Real Texture Evolution Data" submitted for consideration to *Tribology International* is original work conducted by the authors named in the manuscript. We declare that this work has not been previously published, nor is it under consideration for publication elsewhere.

CRediT authorship contribution statement

Yu Yunhong: Writing – original draft, Software, Methodology, Investigation. **You Wu:** Methodology. **Houzhi Wang:** Resources, Funding acquisition. **Wei Huang:** Supervision. **Jun Yang:** Supervision, Funding acquisition. **Yixin Zhou:** Methodology. **Haopeng Wang:** Methodology.

Declaration of Competing Interest

All authors declare that there is no conflict of interest.

Acknowledgments

This research was financially supported by the National Key Research and Development Program of China (No.2021YFB2601200), National Natural Science Foundation of China (No. 52378444, No. 52078130), National Science Fund for Young Scholars of China (No. 52208283), Nanjing Major Science and Technology Project (202405004). This research work is also supported by the Big Data Computing Center of Southeast University. Yunhong Yu was kindly provided financial support by the Chinese Scholarship Council to spend 1 year at Politecnico di Milano, Italy, as part of her doctoral research at Southeast University in Nanjing, China. Therefore, the support of Chinese Scholarship Council was greatly acknowledged.

Data availability

No data was used for the research described in the article.

References

[1] ICAO. Safety report.In, International Civil Aviation Organization, Canada, 2022.
[2] Yang Y, Zhu X, Jelagin D, Guarin A, JvdM Steyn W. Numerical analysis concerning the skid resistance of rubber-contaminated runway grooves. Tribology Int 2021;163:2021.
[3] Yager, T.J. Tire and Runway Surface Research. Presented at Aerospace Technology Conference and Exposition, California, 1986.
[4] Van Es, G. NLR Report-TP-2005-498: Running of runway-Analysis of 3 5 years of landing overrun accidents. National Aerospace Laboratory, Netherland s. ist. psu. edu/viewdoc/download, 2005. 2005.
[5] Thomas D. Can you STOP. AeroSafetyWorld 2011;11:12–5. 2011.
[6] Fwa TF, Chu L. The concept of pavement skid resistance state. Road Mater Pavement Des 2019;22(1):101–20. 2019.
[7] Yu M, You Z, Wu G, Kong L, Liu C, Gao J. Measurement and modeling of skid resistance of asphalt pavement: a review. Constr Build Mater 2020;260:2020.
[8] Zong Y. Study on Tire Mechanics and Aircraft Landing Safety under Wet Pavement Conditions. Tianjin: China Civil Aviation University; 2017.
[9] Yu M, Kong Y, You Z, Li J, Yang L, Kong L. Anti-skid characteristics of asphalt pavement based on partial tire aquaplane conditions. Mater 2022;15(14):2022.
[10] Zhu X, Pang Y, Yang J, Zhao H. Analysis of aircraft tire hydroplaning behavior on real-texture pavement under wet conditions. China J Highw Transp 2020;33(10):159–70. 2020.
[11] Fwa TF, Ong GP. Wet-pavement hydroplaning risk and skid resistance: analysis: proceedings of the american society of civil engineers. J Transp Eng 2008;134(5):182. 2008.
[12] Ong GP, Fwa TF. Wet-pavement hydroplaning risk and skid resistance: modeling. J Transp Eng 2007;133(10):590–8. 2007.
[13] Zhu S, Huang X. Numerical simulation study on hydroplaning speed of tires on transversely grooved concrete pavement. J. Southeast Univ. (Nat. Sci. Ed.) 2016;46(6):1296–300. 2016.
[14] Fwa TF, Kumar SS, Ong GP, Huang CJH. Analytical modeling of effects of rib tires on hydroplaning. Transp Res Rec 2008;2068(1):109–18. 2008.
[15] Jiang B, Chen X, Wang H. Computational analysis of skid resistance of aircraft tire on wet runway pavement with different groove depths. Road Mater Pavement Des 2022;2022:1–18.
[16] Fwa T, Kumar SS, Anupam K, Ong GP. Effectiveness of tire-tread patterns in reducing the risk of hydroplaning. Transp Res Rec 2009;2094(1):91–102. 2009.
[17] Srirangam SK, TF F. Analyzing effect of tire groove patterns on hydroplaning speed. Proceedings of the Eastern Asia Society for Transportation Studies Vol. 7 (The 8th International Conference of Eastern Asia Society for Transportation Studies, 2009). Eastern Asia Society for Transportation Studies; 2009. pp. 377-377.
[18] Liu Y, Chu L, Peng J, Fwa TF. Critical groove depth and width for maintenance management of runway pavements. Int J Pavement Eng 2022;2022:1–11.
[19] Ong G, Fwa T. Modeling skid resistance of commercial trucks on highways. J Transp Eng 2010;136(6):510–7. 2010.
[20] Liu Q, Shalaby A. Simulation of pavement response to tire pressure and shape of contact area. Can J Civ Eng 2013;40(3):236–42. 2013.
[21] Ding Y. Evaluation of hydroplaning risk on permeable friction course using tire–water–pavement interaction model. Transp Res Rec 2018;2672(40):408–17. 2018.
[22] Tang T, Anupam K, Kasbergen C, Scarpas A, Erkens S. A finite element study of rain intensity on skid resistance for permeable asphalt concrete mixes. Constr Build Mater 2019;220:464–75. 2019.
[23] Yang Y, Zhu X, Jelagin D, Guarin A. Smoothed particle hydrodynamics based numerical study of hydroplaning considering permeability characteristics of runway surface. Front Struct Civ Eng 2024;18(3):319–33. 2024.
[24] Zhu X, Pang Y, Yang J, Zhao H. Numerical analysis of hydroplaning behaviour by using a tire–water-film–runway model. Int J Pavement Eng 2020;23(3):784–800. 2020.
[25] Qian J, Wang H. Analysis of skid resistance and braking distance of aircraft tire landing on grooved runway pavement. Int J Pavement Eng 2022;24(2):2022.
[26] Wollny I, Behnke R, Villaret K, Kaliske M. Numerical modelling of tyre–pavement interaction phenomena: coupled structural investigations. Road Mater Pavement Des 2016;17(3):563–78. 2016.
[27] Peng J, Chu L, Fwa TF. Determination of safe vehicle speeds on wet horizontal pavement curves. Road Mater Pavement Des 2020;22(11):2641–53. 2020.
[28] Jiasheng, Y. Tire-pavement noise simulation and analysis.In, 2013.
[29] Yu M, Zhang R, Tang O, Jin D, You Z, Zhang Z. Construction and optimization of asphalt pavement texture characterization model based on binocular vision and deep learning. Measurement 2025;248:116946. 2025.
[30] Yu M, Zhang Z, Chen G, Lv G, Jin D. Investigation of wear resistance performance for asphalt pavement coarse aggregates based on morphological characteristics and mineral composition. Constr Build Mater 2025;491:142752. 2025.
[31] Yu M, Jin D, Liu Y, You Z, Li Y. Performance evaluation of surface treatment waste glass as aggregate in asphalt mixture. Case Stud Constr Mater 2024;21:e03767. 2024.
[32] Srirangam SK, Anupam K, Kasbergen C, Scarpas AT. Analysis of asphalt mix surface-tread rubber interaction by using finite element method. J Traffic Transp Eng (Engl Ed 2017;4(4):395–402. 2017.
[33] Anupam K, Santosh Kumar S, Kasbergen C, Scarpas A, Kane M. Finite element framework for the computation of runway friction of aircraft tires. Transp Res Rec J Transp Res Board 2017;2641(1):126–38. 2017.
[34] Zheng B, Chen J, Zhao R, Tang J, Tian R, Zhu S, et al. Analysis of contact behaviour on patterned tire-asphalt pavement with 3-D FEM contact model. Int J Pavement Eng 2020;23(2):171–86. 2020.
[35] Zhu X, Yang Y, Zhao H, Jelagin D, Chen F, Gilabert FA, et al. Effects of surface texture deterioration and wet surface conditions on asphalt runway skid resistance. Tribology Int 2021;153:2021.
[36] Tan T, Cai W, Xing C, Meng A, Tan Y, She H. Characterization of road surface topography changes during polishing process with characteristic roughness parameter. Wear 2024;550-551:2024.
[37] Yu Y, Wang H, Crispino M, Li Y, Ketabdari M, Xu G, et al. Wear behavior and skid-resistance durability of runway pavements based on surface texture characteristics. Tribology Int 2025;2025:110953.
[38] Tielking JT. Air force engineering & services center.in, air force engineering & services center, Florida. Aircr tire/Pavement Press Distrib 1989.
[39] Kondé AK, Rosu I, Lebon F, Brardo O, Devésa B. On the modeling of aircraft tire. Aerosp Sci Technol 2013;27(1):67–75. 2013.
[40] Yeoh. Some forms of the strain energy function for rubber. Rubber Chem Technol 1993;66(5):754–71. 1993.
[41] Yu Y, Wang H, Wang H, Chen X, Yang J. Texture evolution and skid resistance in polymer-modified asphalt mixtures for runway pavements during wear process. Constr Build Mater 2025;498:144037. 2025.
[42] Hirt C, Nicholls B. Volume of Fluid (VOF) method for dynamics of free boundaries. Comput Phy 1981.
[43] Ahmadzadeh M, Saranjam B, Hoseini Fard A, Binesh AR. Numerical simulation of sphere water entry problem using Eulerian–Lagrangian method. Appl Math Model 2014;38(5-6):1673–84. 2014.
[44] Heinrich G, Klüppel M. Rubber friction, tread deformation and tire traction. Wear 2008;265(7-8):1052–60. 2008.
[45] Kluppel M, Heinrich G. Rubber friction on self-affine road tracks. Rubber Chem Technol 2000;73(4):578–606. 2000.
[46] Li L, Wang KC, Luo W. Pavement friction estimation based on the Heinrich/Klüppel model. Period Polytech Transp Eng 2016;44(2):89–96. 2016.
[47] Fwa T, Ong GP. Wet-pavement hydroplaning risk and skid resistance: analysis. J Transp Eng 2008;134(5):182–90. 2008.
[48] Agrawal, S.K. Braking of an aircraft tire on grooved and porous asphaltic concrete. In, FAA, N.J., 1983.

[49] Rose JG, B. M G. Water depth influence on pavement friction. Transp Eng J ASCE 1977;103(4):491–506. 1977.
[50] Peng W, Li P, Gao J, Liu Z, Wang X, Wang S, et al. Long-term skid resistance evolution and influence mechanism of asphalt pavement based on self-developed wear equipment. Constr Build Mater 2024;453:139085. 2024.
[51] Agrawal SK. The braking performance of an aircraft tire on grooved portland cement concrete surfaces. Washington, D.C.: FAA; 1981.